Regular Article

Majorana bound states in a driven quantum dot

Fabián Medina-Cuy[1,a] , **Dunkan Martínez**[2], **Francisco Domínguez-Adame**[2], **P. A. Orellana**[3]

[1] Dipartamento di Scienza Applicata e Tecnologia, Politecnico di Torino, 10129 Turin, Italy
[2] Departamento de Física de Materiales, GISC, Universidad Complutense, 28040 Madrid, Spain
[3] Departamento de Física, Universidad Técnica Federico Santa María, Casilla 110 V, Valparaíso, Chile

Abstract We study a periodically driven quantum dot in two different configurations. In the first setup, a quantum dot coupled to a topological superconductor and a normal metal lead. In the second setup, a T-shape quantum dot connected to two topological superconductors and side coupled to a normal metal lead. By a combination of non-equilibrium Green's function techniques and Floquet's formalism, we obtain the quasienergy spectra as a function of the amplitude, frequency, and superconducting phase difference. We show that the states develop unique electronic responses, such as the broken particle-hole symmetry that appears when considering the non-locality of Majorana bound states. Finally, we compute the time-average current and the differential conductance to reveal these spectra signatures through physically measurable magnitudes in the two proposed configurations.

1 Introduction

Superconductivity is a phenomenon that recently attracted a lot of attention due to its relevance for quantum computation [1–3]. In a microscopic description of superconducting hybrid junctions, one of the mechanisms that describe the dynamics of carriers is Andreev reflection. The occurrence of multiple Andreev reflections results in the appearance of Andreev bound states (ABS), also known as the Yu–Shiba–Rusinov states [4–7]. ABS can display topological states in multi-terminal Josephson junctions, going beyond the ten-fold way classification, and with applications as qubits [8–10]. Alongside trivial superconductivity, topological superconductivity is also of interest. Specifically, Majorana bound states (MBS) [11, 12] represent an alternative for implementing qubits, since they display non-Abelian statistics with topological protection, thus being robust against decoherence [13–15]. Multi-terminal Josephson junctions with topological superconductors also show topologically protected nodes (zero energy crossings formed by MBS) observed in the parameter space [16–19]. However, before the experimental implementation of MBS as qubits can be developed, achieving a convincing detection of these excitations is crucial. In this context, research in topological superconductivity faces up to the fact that the signatures of MBS and ABS in experiments are rather similar. Theoretical efforts to achieve a better understanding of MBS include the analysis of zero-bias conductance peaks or the detailed analysis of the interferometric measurements [20–23]. From the experimental side, the quest for nearly quantized conductance of non-Majorana states and implementing gap protocols stand out [24, 25].

Periodically driven perturbation in nanostructures provides information on the dynamics of the subgap states, opening the path to Floquet engineering [26, 27] and introducing a whole family of phenomena like space-time crystals [28, 29], Floquet's topological insulators [30], Floquet's chiral [31] and anomalous Floquet's chiral topological superconductors [32]. Such a variety of different phenomena involves the study of symmetries such as rotational, parity, particle-hole, chiral, and time-reversal under a periodic driving [33–35]. Additionally, they bring about selection rules like symmetry-protected dark states, symmetry-protected dark bands, and symmetry-induced transparency [36, 37].

When quantum dot (QD) in a hybrid system QD-topological superconductor is subject to a time-periodic driving, it provides an exciting approach to distinguish ABS from MBS, which consists in generating a double exchange of the MBS at high-frequency [38]. However, the quasiparticle states deserve more attention, especially under MBSs non-locality and the distinguishability with ABS [39, 40]. Therefore, some questions arise: How do Majorana non-locality effects display in the Floquet's spectra? are the zero energy modes robust under driving?, do ABS and MBS behave similarly in the presence of a driving?

Studies of systems like N-QD-S, S-QD-S, S-QD-QD-S, and S-QD-S-QD-S with periodically driven QDs show the behavior of quasiparticle states for trivial superconductivity [41–45] but still remain doubts in the consideration of topological superconductivity. Here, N and S refer to a normal metal and a conventional superconductor, respectively. Following a similar methodology and techniques used in previously mentioned works, here we study the quasiparticle spectra, time-average currents, and differential

---

[a] e-mail: fabian.medina@polito.it (corresponding author)

Fig. 1 Schematic representation of **a** a periodically driven QD coupled to a grounded topological superconductor and a normal metal, referred to as Device A, and **b** periodically driven QD in a T-shape configuration. The QD is between two grounded topological superconductors and side-coupled with a normal metal lead, referred to as Devide B. Red shapes on top of the topological superconductors represent the MBS
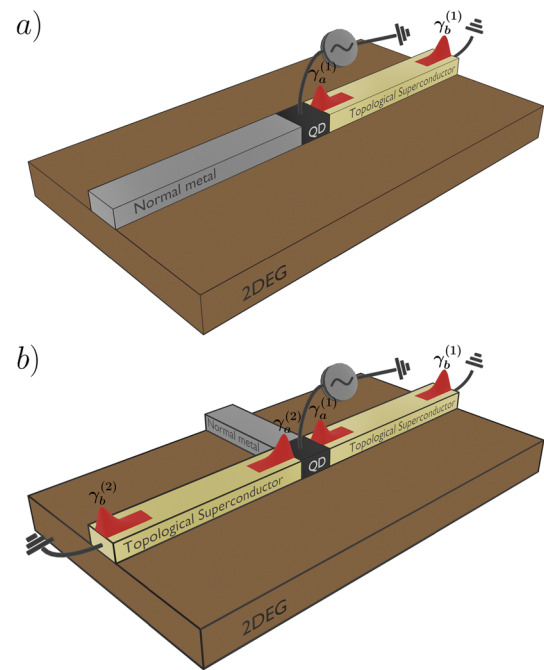
conductance in a TS-QD-N (here, TS stands for topological superconductor) and a T-shape structure with a QD connected to two topological superconductors and a normal metal).

The paper is organized as follows. In Sect. 2, we introduce the model, the Floquet–Green's function formalism, and the time-average currents. Section 3 shows the numerical results of the quasiparticle spectra versus the amplitude and frequency of the driving, time-average currents, and differential conductance for devices A and B depicted in Fig. 1. In Sect. 4, we summarize the results and briefly discuss possible future works.

2 Low energy model and method

2.1 Model Hamiltonian

In this work, we study two different setups. The first one, referred to as Device A in what follows (see Fig. 1a), consists of a QD coupled to a normal metal lead and a topological superconductor, described by a Kitaev chain in its topological phase. The second setup, referred to as Device B hereafter (see Fig. 1b), is formed by a QD coupled to two topological superconductors and one normal metal lead. In either setup, the electron Hamiltonian can be cast in the following form

$$H = H_{QD}(t) + H_N + H_{\text{TS}}^{(1)} + H_{\text{TS}}^{(2)} + H_{C,N} + H_{C,TS}^{(1)} + H_{C,TS}^{(2)}. \tag{1}$$

The time-dependent perturbation enters the QD Hamiltonian given by

$$H_{QD}(t) = \epsilon(t)d^\dagger d \tag{2}$$

with periodic oscillations considered as $\epsilon(t) = \epsilon_d + A\cos(\omega t)$. The creation and annihilation operators for electrons in the QD are $d^\dagger$ and d, respectively. Here, we assume that the system is subject to a magnetic field strong enough so that the Zeeman splitting is large compared to other energy scales. Hence, we can deal with only one spin orientation and regard the QD as spinless. In this way, we disregard Kondo-like effects in the system [46] and the simultaneous coupling of the topological superconductors with two spin channels in the QD [47].

The Hamiltonian for a normal metallic lead reads

$$H_N = \sum_k \xi_{Nk} c_{Nk}^\dagger c_{Nk} \tag{3}$$

where $\xi_{Nk} = \epsilon_{Nk} - \mu_N$, ϵ_{Nk} and μ_N being the energy of an electron with momentum k and the chemical potential of the metallic lead, respectively. $c_{Nk}^\dagger$ and c_{Nk} are the creation and annihilation operators in the metallic lead. The Kitaev Hamiltonian in the topological phase and Majorana representation is expressed as

$$H_{\text{TS}}^\alpha = i\xi_{M,\alpha}\gamma_a^\alpha\gamma_b^\alpha, \tag{4}$$

where the index $\alpha = (1), (2)$ labels the two topological superconductors. The Majorana operators γ_a^α and γ_b^α satisfy the anticommutator $\{\gamma_\kappa^\alpha, \gamma_{\kappa'}^{\alpha'}\} = \delta_{\alpha'\alpha}\delta_{\kappa\kappa'}$, expressed as an equal superposition of electrons and holes, namely $\gamma_a^\alpha = (c_\alpha + c_\alpha^\dagger)/\sqrt{2}$ and $\gamma_b^\alpha = i(c_\alpha - c_\alpha^\dagger)/\sqrt{2}$. Hence, the low-energy effective Hamiltonian in a Dirac fermionic representation is

$$H_{\text{TS}}^\alpha = -\xi_{M,\alpha}\left(c_\alpha^\dagger c_\alpha - \frac{1}{2}\right), \tag{5}$$

where $\xi_M \sim e^{-L/l_0}$, L is the length of the nanowire and l_0 the superconducting coherence length [48] (see Refs. [49, 50] for an explicit expression of the Majorana overlapping in terms of the Rashba strength, Zeeman splitting and superconductor parameters). We consider the overlap energy of the two MBSs as a real number, which means either MBSs interact with each other in the same nanowire or not ($\xi_{M,\alpha} \neq 0$ or $\xi_{M,\alpha} = 0$). The last three terms in the Hamiltonian corresponding to the coupling between the normal metal lead and the two nanowires with the following expressions

$$H_{C,N} = \sum_k \left(t_N c_{Nk}^\dagger d + \text{h.c.}\right). \tag{6}$$

Without losing generality, we chose t_N to be a real number. The coupling between the QD and the topological superconductors is described by the following Hamiltonian

$$H_{C,TS}^\alpha = \left[\lambda_\alpha^- e^{-i\phi_\alpha/2} d^\dagger c_\alpha + \lambda_\alpha^+ e^{-i\phi_\alpha/2} d^\dagger c_\alpha^\dagger + h.c.\right], \tag{7}$$

where $\lambda_\alpha^\pm = (\lambda_\alpha^a \pm \lambda_\alpha^b)/2$ are the couplings of the MBSs with the QD. For a single topological superconductor, the coupling term $H_{C,TS}^{(2)}$ vanishes, and for two topological superconductors, all the Hamiltonian terms remain. Notice that this coupling Hamiltonian provides the nonlocality effects of the MBS [39, 40, 51–53], ϕ_α corresponds to the superconducting phase difference between nanowires—for a single nanowire calculation, we dropped the phase.

2.2 Floquet–Green's functions

The Floquet's formalism is a method for tackling time-periodic systems with a Hamiltonian that satisfies $H(t) = H(t + T)$, with $T = 2\pi/\omega$ being the period of the external driving [54, 55]. Since our interest is the assessment of transport properties (currents and differential conductance), the procedure combines Floquet's approach with Green's function techniques [42–44, 56]. Here, we use Nambu's representation of the Green's functions as a convenient form to express the on-dot paring in the system in terms of spinless propagators

$$\langle\langle\alpha(t)\alpha^\dagger(t')\rangle\rangle = \left\langle\!\!\left\langle \begin{pmatrix} d \\ d^\dagger \end{pmatrix} \otimes \begin{pmatrix} d^\dagger & d \end{pmatrix} \right\rangle\!\!\right\rangle$$
$$= \begin{pmatrix} \langle\langle d(t); d^\dagger(t')\rangle\rangle & \langle\langle d(t); d(t')\rangle\rangle \\ \langle\langle d^\dagger(t); d^\dagger(t')\rangle\rangle & \langle\langle d^\dagger(t); d(t')\rangle\rangle \end{pmatrix}. \tag{8}$$

We implemented the equation of motion method, obtaining Green's function as a set of differential equations and writing them in an integral form on the Keldysh contour. This procedure yields

$$\langle\langle\alpha(t)\alpha^\dagger(t')\rangle\rangle = g_d(t,t') + \int_C dt_1 g_d(t,t_1)\left[t_N\sigma_z\sum_k\langle\langle\zeta_{Nk}(t_1)\alpha^\dagger(t')\rangle\rangle + \sum_\alpha M(\phi_\alpha)\langle\langle\zeta_{\alpha TS}(t_1)\alpha^\dagger(t')\rangle\rangle\right], \tag{9a}$$

$$\langle\langle\zeta_{Nk}(t_1)\alpha^\dagger(t')\rangle\rangle = \int_C dt_2 g_{Nk}(t_1,t_2)t_N\sigma_z\langle\langle\alpha(t_2)\alpha^\dagger(t')\rangle\rangle, \tag{9b}$$

$$\langle\langle\zeta_{\alpha TS}(t_1)\alpha^\dagger(t')\rangle\rangle = \int_C dt_2 g_\alpha(t_1,t_2)M^\dagger(\phi_\alpha)\langle\langle\alpha(t_2)\alpha^\dagger(t')\rangle\rangle, \tag{9c}$$

where $g_d(t,t')$, $g_{Nk}(t_1,t_2)$, $g_\alpha(t_1,t_2)$ are the QD, normal metal lead and topological superconductors bare Green's function, $t_N\sigma_z$ and $M(\phi_\alpha)$ are the tunneling matrices of the metallic lead and the topological superconductors, respectively, with σ_z being the z component of the Pauli matrices. Finally, the anomalous Green's functions for the normal lead and the topological superconductors are $\langle\langle\zeta_{Nk}(t_1)\alpha^\dagger(t')\rangle\rangle$ and $\langle\langle\zeta_{\alpha TS}(t_1)\alpha^\dagger(t')\rangle\rangle$, whose equations of motion are (9b) and (9c). These Green's functions in Nambu's representation are

$$\langle\langle\zeta_\beta(t_1)\alpha^\dagger(t')\rangle\rangle = \left\langle\!\!\left\langle \begin{pmatrix} c_\beta \\ c_\beta^\dagger \end{pmatrix} \otimes \begin{pmatrix} d^\dagger & d \end{pmatrix} \right\rangle\!\!\right\rangle$$
$$= \begin{pmatrix} \langle\langle c_\beta(t); d_\uparrow^\dagger(t')\rangle\rangle & \langle\langle c_\beta(t); d(t')\rangle\rangle \\ \langle\langle c_\beta^\dagger(t); d^\dagger(t')\rangle\rangle & \langle\langle c_\beta^\dagger(t); d(t')\rangle\rangle \end{pmatrix}, \tag{10}$$

where the index $\beta \equiv Nk$, α. Combining Eqs. (9a), (9b) and (9c), we obtain

$$
\langle\langle\alpha(t)\alpha^\dagger(t')\rangle\rangle = g_d(t,t') + \int_C dt_1 dt_2 g_d(t,t_1)
$$
$$
\times \Sigma_\beta(t_1,t_2)\langle\langle\alpha(t_2)\alpha^\dagger(t')\rangle\rangle , \tag{11}
$$

with the self-energy expressed as

$$
\Sigma_\beta(t_1,t_2) = \Sigma_N(t_1,t_2) + \Sigma_{(1)}(t_1,t_2)
$$
$$
+ \Sigma_{(2)}(t_1,t_2) , \tag{12}
$$

where

$$
\Sigma_N(t_1,t_2) = \sum_k t_N^2 g_{Nk}(t_1,t_2) \tag{13}
$$

with

$$
\Sigma_\alpha(t_1,t_2) = M(\phi_\alpha)g_\alpha(t_1,t_2)M^\dagger(\phi_\alpha). \tag{14}
$$

The next step consists of a transformation of the two-time Green's functions and self-energies into a Floquet's representation employing a Wigner transformation (Wigner representation has one-to-one correspondence with Floquet's representation) [55]

$$
\mathcal{F}_{nm}(\epsilon) = \int_{-\infty}^{\infty} dt' \frac{1}{T} \int_0^T dt \, e^{i(\epsilon+n\omega)t - i(\epsilon+m\omega)t'} \mathcal{F}(t,t') \tag{15}
$$

where the energy $\epsilon \in [-\omega/2, \omega/2]$. The transformation is possible since Green's functions have the periodicity of the perturbation in both times. Hence, Eq. (11) provides the Green's function of the QD coupled to the electrodes in Floquet's and Nambu's representation with the result

$$
\langle\langle\alpha(\epsilon)\alpha^\dagger(\epsilon)\rangle\rangle_{nm}^{-1} = g_{d,nm}^{-1}(\epsilon) - \Sigma_{\beta,nm}(\epsilon), \tag{16}
$$

where the Green's function of the bare QD has the form

$$
g_{d,nm}^{r(a)}(\epsilon) = \sum_p \begin{pmatrix} \frac{J_{p-n}\left(\frac{A}{\omega}\right)J_{p-m}\left(\frac{A}{\omega}\right)}{\epsilon \pm i\eta + p\omega + \epsilon_d} & 0 \\ 0 & \frac{J_{p-n}\left(\frac{A}{\omega}\right)J_{p-m}\left(\frac{A}{\omega}\right)}{\epsilon \pm i\eta + p\omega - \epsilon_d} \end{pmatrix}. \tag{17}
$$

The superscript $r(a)$ stands for retarded (advanced) Green's function and $J_l(A/\omega)$ being the Bessel functions of the first kind. In the same manner, we can express the normal metal lead and the topological superconductors self-energies as

$$
\Sigma_{N,nm}^{r(a)}(\epsilon) = \mp \frac{i\Gamma}{2}\sigma_0 \delta_{nm}, \tag{18}
$$

with coupling constant $\Gamma = 2\pi t_N^2 \rho$, σ_0 the two by two unit matrix, and working on the assumption of wide band approximation

$$
\Sigma_{\alpha,nm}^{r(a)}(\epsilon) = \begin{pmatrix} \frac{(\lambda_\alpha^-)^2}{\epsilon \pm i\eta + n\omega - \xi_{M,\alpha}} + \frac{(\lambda_\alpha^+)^2}{\epsilon \pm i\eta + n\omega + \xi_{M,\alpha}} & -\frac{\lambda_\alpha^-\lambda_\alpha^+ e^{-i\phi_\alpha}}{\epsilon \pm i\eta + n\omega - \xi_{M,\alpha}} - \frac{\lambda_\alpha^-\lambda_\alpha^+ e^{-i\phi_\alpha}}{\epsilon \pm i\eta + n\omega + \xi_{M,\alpha}} \\ -\frac{\lambda_\alpha^-\lambda_\alpha^+ e^{i\phi_\alpha}}{\epsilon \pm i\eta + n\omega - \xi_{M,\alpha}} - \frac{\lambda_\alpha^-\lambda_\alpha^+ e^{i\phi_\alpha}}{\epsilon \pm i\eta + n\omega + \xi_{M,\alpha}} & \frac{(\lambda_\alpha^+)^2}{\epsilon \pm i\eta + n\omega - \xi_{M,\alpha}} + \frac{(\lambda_\alpha^-)^2}{\epsilon \pm i\eta + n\omega + \xi_{M,\alpha}} \end{pmatrix} \delta_{nm}. \tag{19}
$$

Note that by shifting the poles with $\epsilon \to \epsilon \pm i\eta$, we obtain the retarded and advanced Green's functions. The self-energy of a normal metal lead Eq. (18) is diagonal in the Nambu's and Floquet's spaces, while the topological superconductors self-energies Eq. (19) are non-diagonal in the Nambu's space and diagonal in the Floquet's space. We consider the Josephson junction at zero bias for these calculations but with a superconducting phase difference between topological superconductors.

2.3 Density of states

The first type of device consists of a QD between a topological superconductor and a metallic lead. The second consists of a QD between two topological superconductors simultaneously coupled to a metallic lead. In what follows, we present the spectra for both devices taking $\epsilon_d = 0$ and $\Gamma/\omega = 0.1$. Furthermore, the calculation of Green's function allows observing the spectrum of a periodically driven QD through the density of states

$$
\langle\rho(\epsilon)\rangle = -\frac{1}{\pi}\sum_n \left(\text{Im}\langle\langle\alpha(\epsilon)\alpha^\dagger(\epsilon)\rangle\rangle_{(11)}^r\right)_{nn}. \tag{20}
$$

The subscript (11) indicates the first element of the Green's function in Nambu's representation and the superscript r stands for the retarded Green's function. Since the amplitude A and frequency ω are the parameters that characterize the driving in the QD, we investigate the spectrum as a function of them.

2.4 Time-average currents

Transport properties such as average-time currents and differential conductance can detect all the spectra hallmarks. Here, we describe the analytical calculations for computing the average currents. Taking the measurements in the normal metal lead with a chemical potential μ_N defined as $I_N(t) = -e\langle \dot{N}_N(t)\rangle$, with $N_N(t) = \sum_k c_{Nk}^\dagger c_{Nk}$. A straightforward calculation leads to the expression.

$$I_N(t) = \frac{2e}{\hbar} \sum_k \mathrm{Re}\big\{ t_N \sigma_z \langle\langle \zeta_{Nk}(t) d(t)\rangle\rangle^< \big\}_{(11)}, \tag{21}$$

with $\langle\langle c_{Nk}(t) d^\dagger(t)\rangle\rangle^< = i\langle c_{Nk}(t) d^\dagger(t)\rangle$. Making use of Langreth's rules, the time-dependent current is calculated as follows

$$\begin{aligned} I_N(t) = \frac{2e}{\hbar} \int dt_1 \mathrm{Re}\big\{ &\langle\langle \alpha(t)\alpha^\dagger(t_1)\rangle\rangle^r \Sigma_N^<(t_1, t) \\ &+ \langle\langle \alpha(t)\alpha^\dagger(t_1)\rangle\rangle^< \Sigma_N^r(t_1, t) \big\}_{(11)}. \end{aligned} \tag{22}$$

In Floquet's representation and taking the average over a period T, one gets

$$\begin{aligned} \langle I_N\rangle = \frac{2e}{h} \int\limits_{-\omega/2}^{\omega/2} d\epsilon \, \mathrm{Tr}\big[\mathrm{Re}\big\{ &\langle\langle \alpha(\epsilon)\alpha^\dagger(\epsilon)\rangle\rangle^r \Sigma_N^<(\epsilon) \\ &+ \langle\langle \alpha^\dagger(\epsilon)\alpha(\epsilon)\rangle\rangle^< \Sigma_N^a(\epsilon)\big\}_{(11)}\big], \end{aligned} \tag{23}$$

where the trace runs over the Floquet's and Nambu's spaces. The lesser Green's function and self-energy are

$$\begin{aligned} \langle\langle \alpha(\epsilon)\alpha^\dagger(\epsilon)\rangle\rangle^< = &\langle\langle \alpha(\epsilon)\alpha^\dagger(\epsilon)\rangle\rangle^r \Sigma_\beta^<(\epsilon) \\ &\times \langle\langle \alpha(\epsilon)\alpha^\dagger(\epsilon)\rangle\rangle^a , \end{aligned} \tag{24}$$

with

$$\Sigma_\beta^<(\epsilon) = \Sigma_N^<(\epsilon) + \Sigma_{(1)}^<(\epsilon) + \Sigma_{(2)}^<(\epsilon) \tag{25}$$

and

$$\Sigma_\beta^<(\epsilon) = \big(\Sigma_\beta^a(\epsilon) - \Sigma_\beta^r(\epsilon)\big) f_\beta(\epsilon) \tag{26}$$

where $f_\beta(\epsilon)$ is the Fermi distribution function for the β leads. We take the zeroth-order component of the current at zero temperature for all numerical calculations.

3 Numerical results

3.1 Device A

3.1.1 Amplitude and frequency Floquet spectra

We drop the superconducting phase difference and the subscript α in the self-energy Eq. (19) in the case of Device A (see Fig. 1a). Figure 2 displays the average density of states calculated from Eq. (20). Here, the spectrum is obtained by the relation of the quasiparticle energy ϵ/ω and the amplitude A/ω (amplitude spectrum), with $\lambda^a/\omega = 1$, truncating the Floquet's harmonics at $|n| = 3$. In Fig. 2a, a single MBS tunnels through the QD, meaning that $\lambda^b/\omega = 0$ and $\xi_M/\omega = 0$. The zeroth harmonic component remains independent of the amplitude and is present in the higher harmonics gaining and losing weight with the increasing amplitude. For small values of amplitude (about $A < 3$ as it shows in the spectrum), the quasiparticles display crossing energy states, while for larger values of amplitude ($A > 3$), the quasiparticle display avoids energy crossing. Figure 2b shows the spectrum for two MBSs hybridizing with the QD state, but they do not overlap in the nanowire, meaning that $\xi_M/\omega = 0$—physically, this configuration could correspond to a ring structure of the topological superconductor [57]. In this situation, the state at zero energy splits into two particle-hole symmetric states away from zero energy, and exactly as in the previous scenario the splitting replicates in higher harmonics. Figure 2c, the two MBSs hybridize with the QD state, and both are interacting through the nanowire, meaning that $\lambda^b/\omega = 1$, $\lambda^a/\omega = 0.5$ and $\xi_M/\omega = 0.6$. The two branches around $n = 0$ show a noticeable difference in their weights, a

Fig. 2 Amplitude spectra in Device A obtained for the four possible types of hybridization of the Majoranas with the QD. Parameters are $\lambda^a/\omega = 1$ and $\Gamma/\omega = 0.1$
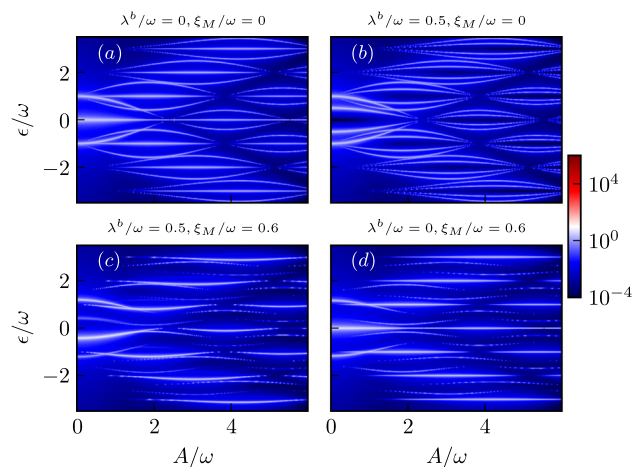
Fig. 3 Frequency spectra in Device A obtained for the four types of possible hybridization of the Majoranas with the QD. Parameters are $A/\lambda^a = 2.5$ and $\Gamma/\lambda^a = 0.1$
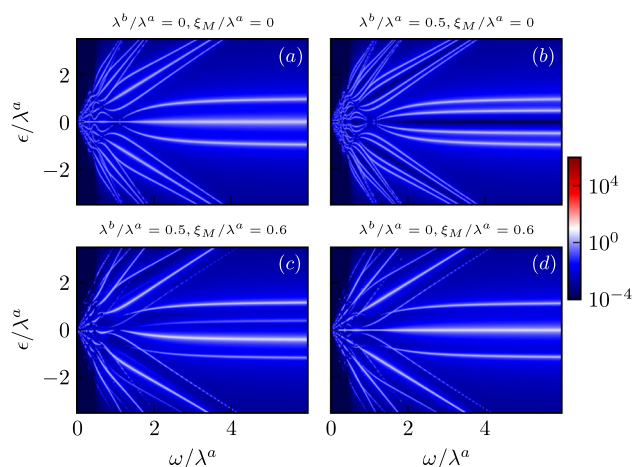
coupling configuration of the MBSs that breaks particle-hole symmetry. Figure 2d, a single MBS is hybridizing with the QD state and displays an overlap of MBSs in the nanowire. Here, a zero energy state independent of the amplitude appears and replicates for higher harmonics, but the splitting structure of the quasiparticle energy states shown in panels (a) and (b) disappears.

Figure 3 shows the average density of states (20). Here, we plot the quasi-energy ϵ/λ^a related to the driving frequency ω/λ^a (frequency spectrum). For these spectra, we fix the amplitude to the value $A/\lambda^a = 2.5$, the coupling with the normal metal is set at $\Gamma/\lambda^a = 0.1$ and the coupling configurations of the MBSs to the QD are the same as for the amplitude spectra shown in Fig. 2 (one MBS hybridized with the QD state, two MBSs hybridized with the QD state but without overlap, two MBSs hybridized with the QD state and overlap between them, and one MMS hybridized with the QD state with overlap between them, plotted, respectively, in panels (a), (b), (c) and (d)). Here, panels (a) and (b) show energy branch oscillations at low frequencies, and in the limit of high frequency all spectral weight concentrates in three (in the case of panel (a) two equidistant states and one at zero energy) and four (in the case of panel (b)). The zero energy state appears independent of the frequencies in panel (a). In higher-order harmonics, the states split into three branches, with the middle being linearly related to frequency. In panel (b), the two Majoranas hybridizing QD produce two branches with symmetrical weights around zero energy (particle-hole symmetric). Panel (c) shows non-symmetric weights of the energy states meaning the broken particle-hole symmetry and no branch oscillations at the approaching zero frequency limit. Finally, in panel (d) appears the zero energy state independent of the frequencies, and no energy branch oscillations in the limit of low frequency. For the non-locality effects of the MBSs in QDs, see [40, 51] and for the couplings in quantum rings [53]. Additionally, we can compare the results of this subsection with a recent work that considers a similar set-up but with trivial instead of topological superconductivity [41], see Sect. 3.1.3.

3.1.2 Subgap time-average current and differential conductance (Device A)

We calculate the subgap currents of Device A in the metal lead with a detuning chemical potential $\mu_N = \mu_{TS} + eV$, with the topological superconductor grounded, we have $\mu_{TS} = 0$. We use the same parameters used in Sect. 3 to calculate currents in this section.

Fig. 4 Device A time-average currents (**a**)–(**d**) (each panel corresponding, respectively, with the spectra in Fig. 2) and differential conductance (**e**)–(**h**) obtained for two values of amplitude $A/\omega = 1, 2$ and taking negative bias ($V < 0$)
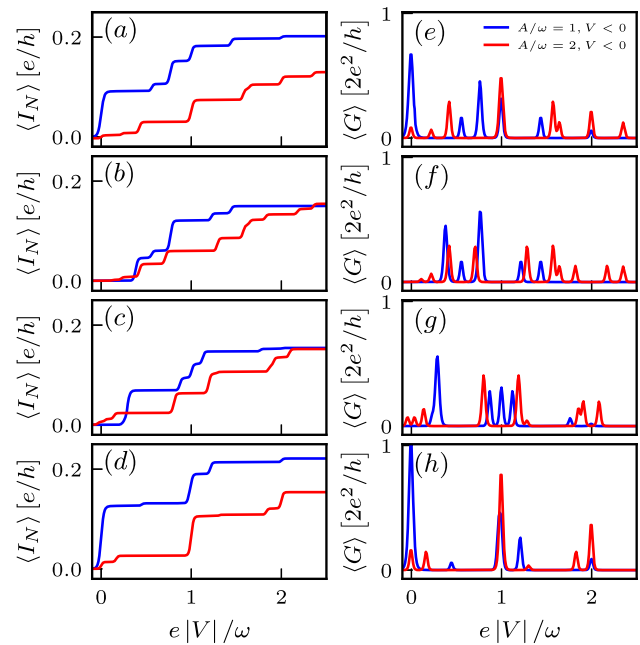

Figure 4 shows the average currents (left panels) and differential conductance (right panels), where blue and red lines correspond to currents and differential conductance for amplitudes $A/\omega = 1$ and $A/\omega = 2$, respectively, with a negative bias applied to the system μ_N^-. Each plateau in the currents corresponds to a saturation of an energy state, meaning that each step corresponds to the presence of a quasiparticle energy state and the peaks in the differential conductance coincide with the states for the amplitude spectra in Fig. 2. Since we are in the low energy limit and considering spinless superconductivity, we expect only contributions of the orders of $2e^2/h$ in the differential conductance. Hence, in the limit of zero amplitude ($A = 0$) and strong coupling of the QD with the metallic lead, we recovered the known results in the case of a nanowire coupled to the QD [46, 58].

3.1.3 Setup of Device A with a BCS superconductor

We focused here on a reproduction of some of the results reported in [41] for comparison purposes. Notice that Green's function in the Nambu's notation varies from Eq. (8). The reason lies in the fact that for a BCS superconductor, we consider the two spins degrees of freedom, while in the case of a p-wave, we have fully polarized spins. Therefore, the Green's function in the Nambu's representation writes as

$$
\langle\langle \alpha(t)\alpha^\dagger(t')\rangle\rangle = \left\langle\!\!\left\langle \begin{pmatrix} d_\uparrow \\ d_\downarrow^\dagger \end{pmatrix} \otimes \left(d_\uparrow^\dagger \; d_\downarrow \right) \right\rangle\!\!\right\rangle
$$
$$
= \begin{pmatrix} \langle\langle d_\uparrow(t); d_\uparrow^\dagger(t')\rangle\rangle & \langle\langle d_\uparrow(t); d_\downarrow(t')\rangle\rangle \\ \langle\langle d_\downarrow^\dagger(t); d_\uparrow^\dagger(t')\rangle\rangle & \langle\langle d_\downarrow^\dagger(t); d_\downarrow(t')\rangle\rangle \end{pmatrix}. \tag{27}
$$

The expression to obtain the average density of states will remain the same as Eq. (20). In Fig. 5, panel (a) shows the average amplitude spectrum (quasiparticle energy versus the amplitude of the driving) with $\Gamma_{sc}/\omega = 1$, panel (b) shows the frequency spectrum (quasiparticle energy versus the frequency of the driving) fixing the amplitude at $A/\Gamma_{sc} = 2.5$. Panel (c) shows the average currents for two different amplitudes (blue line for amplitude $A/\omega = 2$ and red line for amplitude $A/\omega = 0$), the steps coincide with the energy states of panel (a), and finally, panel (d) shows the average differential conductance for the same two values of amplitude. Notice, here the differential conductance in units of $4e^2/h$ corresponds to a Cooper pair and the consideration of the two spin degrees of freedom.

We took the infinite gap limit ($\Delta \rightarrow \infty$) in the self-energy and used Eq. (18) to reproduce the data in Fig. 5. Said that the self-energy for the BCS superconductor in the infinite gap limit is off-diagonal and written as

$$
\Sigma_{sc}^{nm}(\epsilon) = \frac{\Gamma_{sc}}{2}\sigma_x \delta_{nm}, \tag{28}
$$

where Γ_{sc} is the coupling with the superconducting lead and σ_x the x component of the Pauli matrices. The difference between the self-energy Eq. (19) and the self-energy Eq. (28) is that the first depends on the Floquet's harmonics as $1/n\omega$, while the second is independent of another characteristic is that for BCS superconductivity we integrate out over all degrees of freedom while in the case of effective coupling of MBSs we do not.

Fig. 5 Amplitude and frequency spectra panel (**a**) and (**b**) for a driven QD in between a normal metal and a superconducting lead. Average current and differential conductance panels (**c**) and (**d**). The parameters used for each panel are: (**a**) $\Gamma_{sc}/\omega = 1$, in (**b**) $A/\Gamma_{sc} = 2.5$, in the case of panel (**b**) $\Gamma_N/\Gamma_{sc} = 0.1$, and for all panels $\Gamma_N/\omega = 0.1$
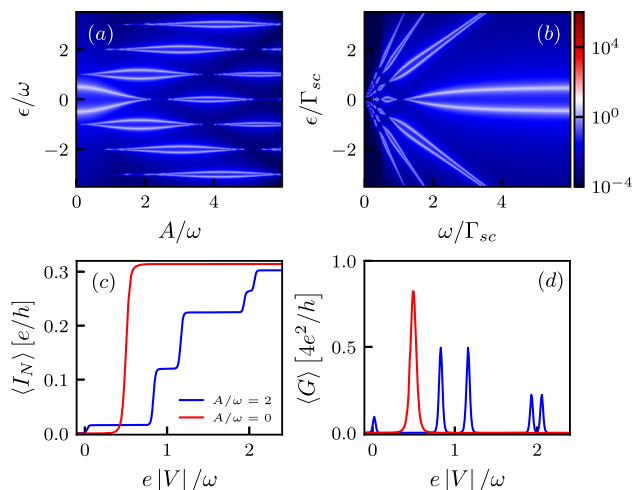
Fig. 6 Schematic representation of MBS possible couplings with the QD in Device B. For the values $\lambda^a_{(1)} = \lambda^a_{(2)} = 1$, $\xi_{M,(1)} = \xi_{M,(2)} = 0.6$ and $\lambda^b_{(1)} = \lambda^b_{(2)} = 0.5$. We use these parameters for all spectra and currents data—the same order of the panels with the couplings in this figure remains for Figs. 7, 8, 9, 10 and 11
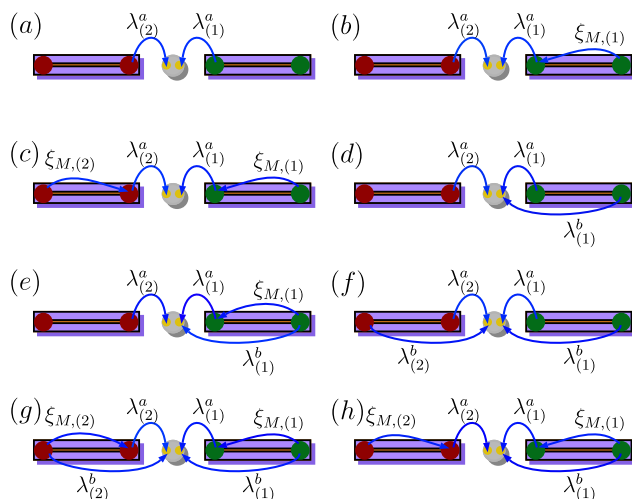
3.2 Device B

Device B is the most basic structure to implement a fusion of MBS [59–61], but those considerations go beyond this work. Here, we want to understand the dynamics of the subgap quasiparticles and observe the difference with ABS. Therefore, we concentrate on the characteristics of the Floquet's spectra and the transport properties of this device. The schematic representation of Device B is shown in Fig. 1b and the coupling configurations of the MBS in Fig. 6, where each panel corresponds to a single type of coupling configuration used for calculating spectra, currents, and differential conductance. Before analyzing the amplitude and frequency spectra, it is important to observe the Andreev spectrum, which is the quasiparticle energy related to the superconducting phase difference ϕ. Similarly to Device A, we will perform the calculations with the setup of Device B but consider BCS superconductivity.

3.2.1 Andreev–Floquet spectra

To observe more clearly the behavior of the states in the Andreev spectrum, we chose the first two Floquet's Harmonics $|n| = 2$ to plot with amplitude $A/\omega = 1$, where at this amplitude, only lower harmonics develop. We can observe the splinting of states as a function of the superconducting phase difference—explicitly, the phase difference is $\phi = \phi_L - \phi_R$, with $\phi_{L(R)}$ the phase of the left and right topological superconductor, respectively, for all numerical results we fixed $\phi_R = 0$.

   Figure 7 shows the Andreev spectra for each coupling configuration shown in Fig. 6. Starting with panels (a), (d), and (f), those correspond to the configurations in which the outer and inner MBS do not overlap with each other in the nanowires, meaning $\xi_{M\alpha} = 0$. Note that no zero energy state is formed. In panel (a), there is only zero energy crossing states every 2π while in panels (d) and (f), the states around zeroth-order harmonic form avoided crossings at $\phi = 0$ and $\phi = 2\pi$ this is due to the interaction of MBSs hybridized the QD state. Panels (b), (c), and (e) correspond to coupling configuration in which inner and outer MBSs overlap. Here, the spectrum at zeroth-order harmonic shows a state independent of the phase. Lastly, in panels (e), (g) and (h) where the hybridization of the outer and inner MBSs with the QD state is present together with MBS overlapping, the weight of states in

Fig. 7 Andreev spectra for the average density of states. We fixed the amplitude of the driving at $A/\omega = 1$. Panels (**e**), (**g**) and (**h**) show broken particle-hole symmetry. The spectrum in each panel coincides with the configurations sketched in the panels of Fig. 6
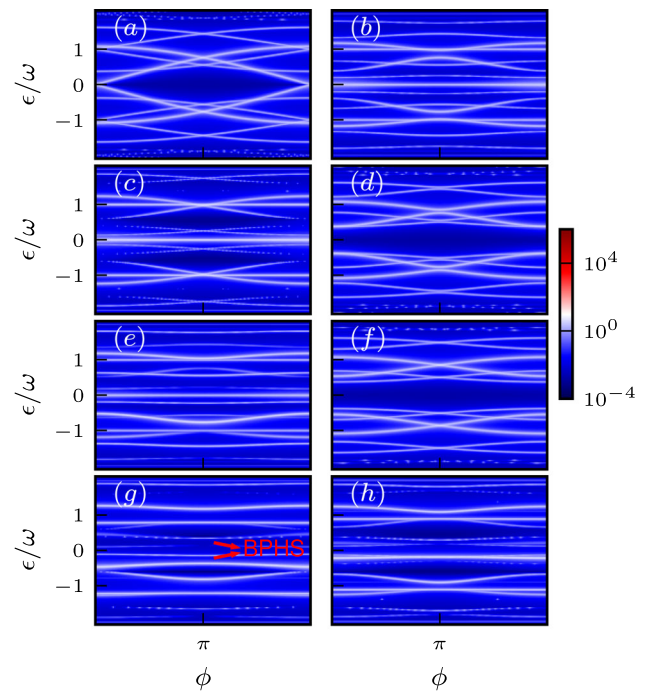
positive and negative harmonics is asymmetrical. This situation is similar to what Device A shows in panels (c) of Figs. 2 and 3. It is a signature of broken particle-hole symmetry observed for the Floquet–Andreev spectrum. Thus, panels (e), (g) and (h) show broken particle-hole symmetry, quite notoriously around $\phi = \pi$—in what follows, we work at this value of phase difference, where we find most marked differences of Devices A and B.

3.2.2 Amplitude and frequency Floquet spectra

Device B for arbitrary values of the superconducting phase difference displays similar behavior in the amplitude and frequency spectra to those observed in Device A (the states in each harmonic splits in two and develop similar with amplitude and frequency), except for a superconducting phase difference of $\phi = \pi$ also is a point at which is more notorious the breaking of particle-hole symmetry. Therefore, we studied amplitude and frequency spectra for that specific phase value.

Figure 8 shows the amplitude spectra for the couplings described in Fig. 6. The salient aspect of these spectra is in most cases, and there is no presence of zero energy state, rather two branches splits for each harmonic gains and loses weight with the amplitude—being at a phase difference of $\phi = \pi$ is the reason to observe no zero energy state in each harmonic. Hence, only two branches of quasiparticle energies split, observing crossing quasiparticle energy states for low amplitude and avoiding energy crossings for large amplitude seen in panels (a), (d), and (f). Panel (c) shows the destruction of the two branch structure in each harmonic (let us remember that for this spectrum $\xi_{M,(1)} = \xi_{M,(2)} \neq 0$). Panels (**b**) and (e) are obtained for couplings configurations in which one nanowire is infinite long, while the other is finite, meaning $\xi_{M,(1)} \neq 0, \xi_{M,(2)} = 0$. These spectra show an overlapping between two spectra, the panel (a)-like spectrum and the panel (c)-like spectrum, observing in (e) a slightly broken particle-hole symmetry. Panels (e), (g) and (h) are the special cases in which particle-hole symmetry breaks, most notoriously at (g) and (h).

Figure 9 shows the frequency spectra for each coupling configuration shown in Fig. 6. Similar to what is shown in Fig. 8, panels (a), (d) and (f) at $\phi = \pi$ do not show a significant difference between them—the common characteristic is that the hybridization between Majoranas bound states in the nanowires is zero ($\xi_{M,(1/2)} = 0$). Panels (b), (c) and (e) all of them have the presence of a zero energy state independent of frequency being a robust state since it is also independent of amplitude as well as superconducting phase difference. Surprisingly, this state remains in conditions of a broken particle-hole symmetry as it is the case of panel (e) and it replicates for all harmonics. Again, the spectra in panels (g) and (h) show broken particle-hole symmetry, but the zero energy states completely disappeared. Therefore, multiple MBSs in the QD with overlapping between them produce a particle-hole broken spectrum. Last aspect to underline is the destruction of oscillations at low-frequency limit when the two topological superconductors have a finite length (panels (c), (g) and (h) show this fact).

3.2.3 Subgap time-average current and differential conductance in Device B

Similar to the previous scenario, we calculated the subgap currents for Device B in the metallic lead with a chemical potential μ_N. Grounding the two topological superconductors yields $\mu_{\text{TS}}^{(1)} = \mu_{\text{TS}}^{(2)} = 0$. The superconducting phase difference is a function of

Fig. 8 Amplitude spectra for
Device B for $\lambda^a_{(2)} = \lambda^a_{(1)} = 1$,
$\Gamma/\omega = 0.1$ and $\phi = \pi$ for all
plots. Each panel corresponds to
the couplings configurations
shown in Fig. 6
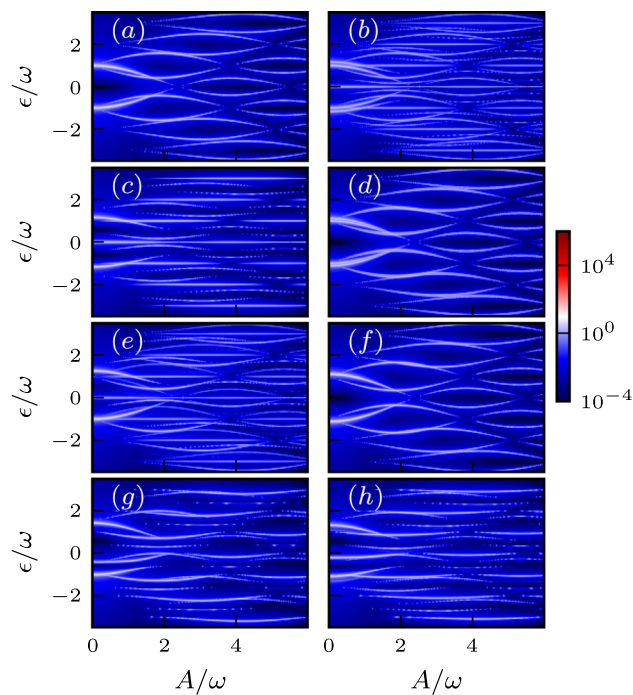
Fig. 9 Frequency spectra for
Device B for $A/\lambda^a_{(1)} = 2.5$,
$\lambda^a_{(2)} = \lambda^a_{(1)} = 1$ and $\Gamma/\lambda^a_{(1)} = 0.1$
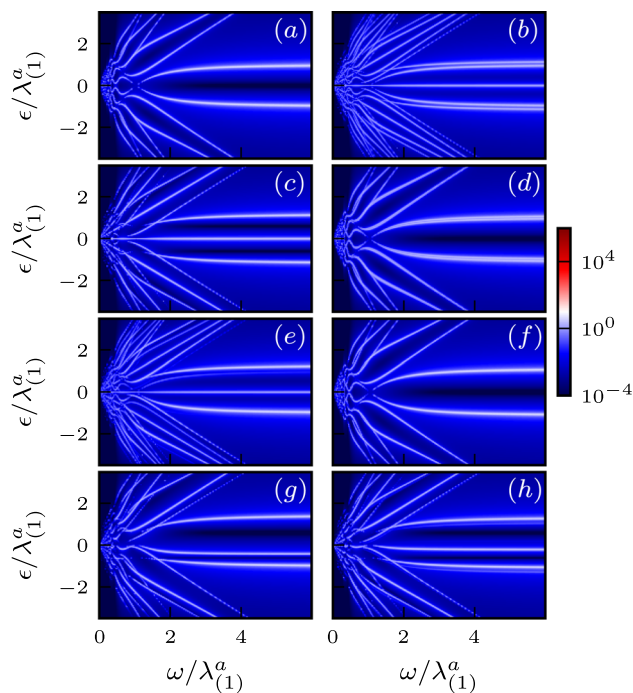
time $\phi(t) = \phi + eVt$. Hence, as we consider grounded topological superconductors, the voltage drop between them vanishes, and
the superconducting phase difference becomes a parameter independent of time. Figure 10 shows the currents in Device B for two
values of superconducting phase difference, being $\phi = 0$ and π represented by blue and green curves with a negative bias applied
($V < 0$). Specifically, in panels (g), the curves for positive bias ($V > 0$) represented by dashed cyan and light green curves with
the superconducting phase difference values $\phi = 0$ and π, respectively. We can notice the mismatch of the curves for the negative
bias and positive bias indicating the broken particle-hole symmetry—let us recall that the amplitude value is at $A/\omega = 1$, and the
currents from each panel correspond, respectively, to the coupling configurations described in Fig. 6.

The differential conductance can detect the quasiparticle energy states and their splittings, and it provides a measurement of
the distribution of the spectral weights for each harmonic. Therefore, we can compute the differential conductance with the data
for the current as $\langle G \rangle = d\langle I_N \rangle / d\mu_N$. Figure 11 shows the differential conductance for the currents shown in Fig. 10, where one

Fig. 10 Device B average currents (each panel corresponding, respectively, with spectra in Fig. 8) obtained for $A/\omega = 1$ and taking multiple values of superconducting phase difference, the bias is considered for negative and positive values ($V < 0$, $V > 0$)
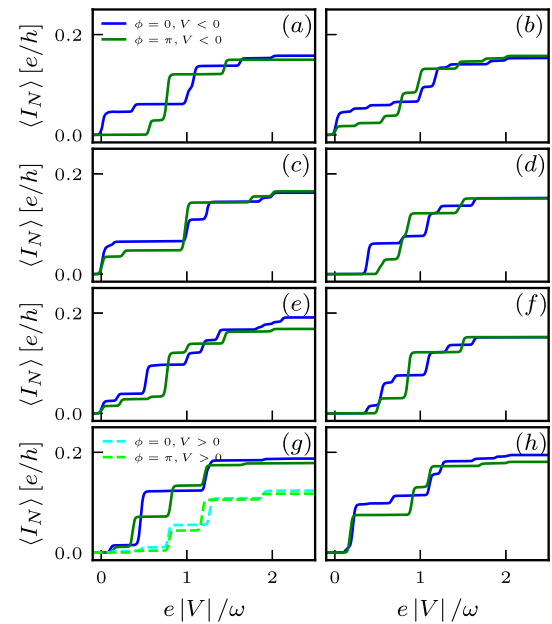
Fig. 11 Device B average differential conductance (each of the panels corresponding, respectively, with the currents in Fig. 10)
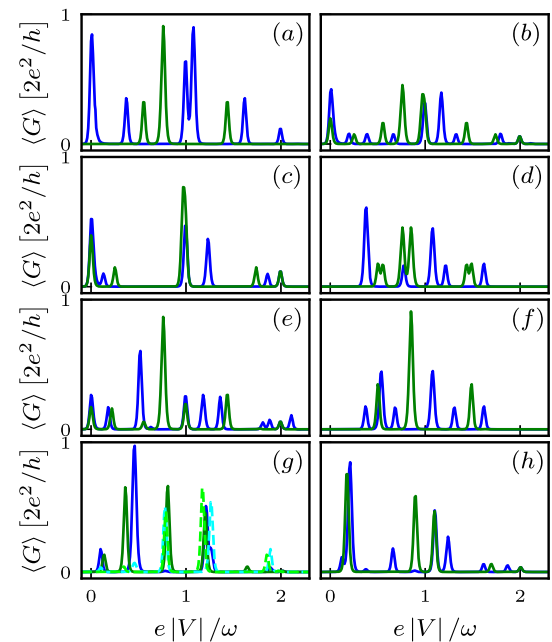
notorious characteristic in panels (b), (d) and (h) is the splitting of the two states that start near harmonic $n = \pm 1$, represented by the green lines. This splitting of the states is difficult to notice in the amplitude spectra and the currents, but it is nicely observed in the differential conductance—see panels (b), (d) and (h) in Fig. 7 the double peak corresponds to an avoiding crossing of states near harmonic $n = \pm 1$. This double peak appears for the coupling configurations with an odd number of MBSs hybridized with the QD state at a value of phase difference $\phi = \pi$ (directly or indirectly)—see also panels (b), (d) and (h) in Fig. 6.

3.2.4 Device B with BCS superconductors

The calculation of spectra, currents, and differential conductance for a driven QD coupled to two superconductor leads and a metal lead is similar to the previous case. The imaginary part of Green's function (27) provides the density of states, and the same formalism described before gives the currents measured in the normal metal lead. The only aspect that changes is the self-energy, which in the infinite gap limit reads.

$$\Sigma_{sc,\alpha}^{nm}(\epsilon) = \frac{\Gamma_{sc}}{2}\begin{pmatrix} 0 & e^{-i\phi_\alpha} \\ e^{i\phi_\alpha} & 0 \end{pmatrix}\delta_{nm},\tag{29}$$

Fig. 12 Amplitude, frequency, and Andreev spectra for a driven QD attached to two superconductors and normal metal leads. Panels (**a**) and (**b**) are obtained for a superconducting phase difference of $\phi = \pi$, panel (**b**) is obtained for an amplitude $A/\Gamma_{sc} = 2.5$, while panel (**c**) is obtained for $A/\omega = 1$. Panels (**d**) and (**e**) are the average currents and differential conductance with a fixed amplitude $A/\omega = 1$. $\Gamma_N/\Gamma_{sc} = 0.1$ is used in panel (**b**), and $\Gamma_N/\omega = 0.1$ is used in the rest of the panels
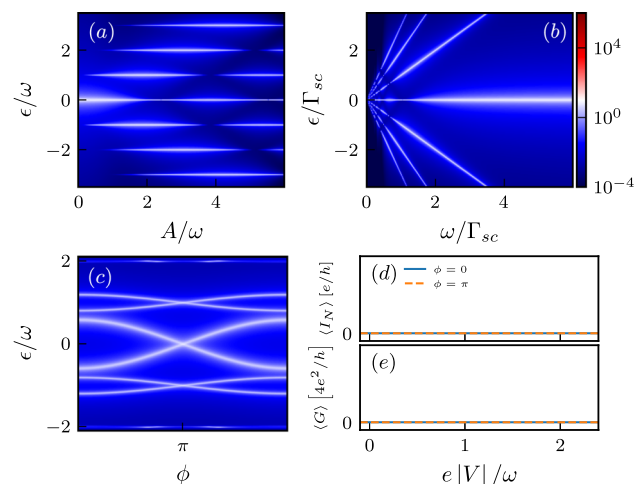
with $\Gamma_L = \Gamma_R = \Gamma_{sc}$ being a symmetric coupling between the superconductors, ϕ_α is the superconducting phase in lead α. Here, we assume a grounded superconductor, and the bias between them is zero. Figure 12 shows the amplitude spectrum panel (a), frequency spectrum (b) and the Andreev spectrum (c). In the former two spectra, we chose a superconducting phase difference of $\phi = \pi$, where for this specific point, the spectra present no splitting of the states around each harmonic—panels (a) in the spectra for device B correspond to the symmetric coupling of the topological superconductors. Panel (c) shows the Andreev spectra obtained for $A/\omega = 1$. Note that exactly at $\phi = \pi$ the spectrum displays crossing states. Panels (d) and (e) correspond to the average current and differential conductance, respectively, for two values of superconducting phase difference $\phi = 0$ and π, lines blue and dashed orange, respectively. The very small magnitude of currents and differential conductance is due to the leak of electrons into superconductors very rapidly [62]—Notice, for device B with topological superconductors, this is not true.

4 Summary

We studied a low-energy model for a periodically driven QD in the presence of MBS, which describes two devices named A and B. The first consists of a QD coupled to a normal metal lead and a topological superconductor. The second is a T-shape structure of a QD connected between two topological superconductors and the side-coupled normal metal lead. Besides, we considered the non-locality of the MBS for both devices.

Device A shows quasiparticle energy states that split in two and repeat for each Floquet's harmonic, accompanying them a flat energy state or an internal splitting of another two states (this depends on the type of hybridization of the MBSs with the QD). Another characteristic in the spectra is the breaking of particle-hole symmetry that occurs when two MBSs hybridize with the QD state and simultaneously interact between them—even though it is true that particle-hole symmetry breaks equally for an undriven system ($A/\omega = 0$), it destroys the oscillations of quasiparticle states for all Floquet's harmonics.

For Device B, the presence of two topological superconductors allows us to observe the quasiparticle states of the superconducting phase difference. Hence, we focused on $\phi = \pi$ for observing the amplitude and frequency spectra—especially for the unique behavior that the states develop at that value and the differences with Device A. Here, whenever we have only direct hybridization of the MBSs with the QD (meaning $\xi_{M,(1/2)} = 0$) the spectra show no zero energy mode. We also observed that for a coupling configuration, (e) (see Fig. 6), even with a broken particle-hole symmetry spectrum, exists a zero energy state. This is possible because one of the topological superconductors breaks particle-hole symmetry while the other stills preserve it.

To detect the broken particle-hole symmetry as well as other characteristics that the quasiparticles display, we propose swapping the bias voltage for negative to positive values ($V < 0$, $V > 0$) where, under broken particle-hole symmetry conditions, the mismatch between the current curves is also seen in the differential conductance.

Coulomb interaction in the QD might originate a further development of the states—for considering electron–electron interaction, we should drop off the consideration of the strong Zeeman field we did at the beginning of the work, and we cannot avoid the Kondo problem. Another interesting consideration is the inclusion of non-Hermitian Hamiltonians to observe differences between ABSs and MBSs [63, 64]. These interactions provide relevant ways to uncover the differences between ABS and MBS in systems under time-periodic driving.

Data Availability Statement No data associated in the manuscript.

References

1. H.-L. Huang, D. Wu, D. Fan, X. Zhu, Superconducting quantum computing: a review. Sci. China Inf. Sci. **63**, 180501 (2020). https://doi.org/10.1007/s11432-020-2881-9
2. J.M. Gambetta, J.M. Chow, M. Steffen, Building logical qubits in a superconducting quantum computing system. NPJ Quantum Inf. **3**, 2 (2017). https://doi.org/10.1038/s41534-016-0004-0
3. J. Clarke, F.K. Wilhelm, Superconducting quantum bits. Nature **453**, 1031 (2008). https://doi.org/10.1038/nature07128
4. B. Pannetier, H. Courtois, Andreev reflection and proximity effect. J. Low Temp. Phys. **118**, 599 (2000). https://doi.org/10.1023/A:1004635226825
5. A. Odobesko, D. Di Sante, A. Kowalski, S. Wilfert, F. Friedrich, R. Thomale, G. Sangiovanni, M. Bode, Observation of tunable single-atom Yu–Shiba–Rusinov states. Phys. Rev. B **102**, 174504 (2020). https://doi.org/10.1103/PhysRevB.102.174504
6. A. Jellinggaard, K. Grove-Rasmussen, M.H. Madsen, J. Nygård, Tuning Yu–Shiba–Rusinov states in a quantum dot. Phys. Rev. B **94**, 064520 (2016). https://doi.org/10.1103/PhysRevB.94.064520
7. L. Pavešić, R. Žitko, Qubit based on spin-singlet Yu–Shiba–Rusinov states. Phys. Rev. B **105**, 075129 (2022). https://doi.org/10.1103/PhysRevB.105.075129
8. R.-P. Riwar, M. Houzet, J.S. Meyer, Y.V. Nazarov, Multi-terminal Josephson junctions as topological matter. Nat. Commun. **7**, 11167 (2016). https://doi.org/10.1038/ncomms11167
9. N. Pankratova, H. Lee, R. Kuzmin, K. Wickramasinghe, W. Mayer, J. Yuan, M.G. Vavilov, J. Shabani, V.E. Manucharyan, Multiterminal Josephson effect. Phys. Rev. X **10**, 031051 (2020). https://doi.org/10.1103/PhysRevX.10.031051
10. H.-Y. Xie, M.G. Vavilov, A. Levchenko, Topological Andreev bands in three-terminal Josephson junctions. Phys. Rev. B **96**, 161406 (2017). https://doi.org/10.1103/PhysRevB.96.161406
11. K. Flensberg, Tunneling characteristics of a chain of Majorana bound states. Phys. Rev. B **82**, 180516 (2010). https://doi.org/10.1103/PhysRevB.82.180516
12. K. Laubscher, J. Klinovaja, Majorana bound states in semiconducting nanostructures. J. Appl. Phys. **130**, 081101 (2021). https://doi.org/10.1063/5.0055997
13. C. Schrade, L. Fu, Majorana superconducting qubit. Phys. Rev. Lett. **121**, 267002 (2018). https://doi.org/10.1103/PhysRevLett.121.267002
14. T. Karzig, W.S. Cole, D.I. Pikulin, Quasiparticle poisoning of Majorana qubits. Phys. Rev. Lett. **126**, 057702 (2021). https://doi.org/10.1103/PhysRevLett.126.057702
15. J.F. Steiner, F. von Oppen, Readout of Majorana qubits. Phys. Rev. Res. **2**, 033255 (2020). https://doi.org/10.1103/PhysRevResearch.2.033255
16. M. Houzet, J.S. Meyer, Majorana–Weyl crossings in topological multiterminal junctions. Phys. Rev. B **100**, 014521 (2019). https://doi.org/10.1103/PhysRevB.100.014521
17. L. Peralta Gavensky, G. Usaj, C.A. Balseiro, Topological phase diagram of a three-terminal Josephson junction: from the conventional to the Majorana regime. Phys. Rev. B **100**, 014514 (2019). https://doi.org/10.1103/PhysRevB.100.014514
18. F. Medina, J.P. Ramos-Andrade, L. Rosales, P. Orellana, Josephson and persistent currents in a quantum ring between topological superconductors. Ann. Phys. **533**, 2100305 (2021). https://doi.org/10.1002/andp.202100305
19. K. Sakurai, M.T. Mercaldo, S. Kobayashi, A. Yamakage, S. Ikegaya, T. Habe, P. Kotetes, M. Cuoco, Y. Asano, Nodal Andreev spectra in multi-Majorana three-terminal Josephson junctions. Phys. Rev. B **101**, 174506 (2020). https://doi.org/10.1103/PhysRevB.101.174506
20. T.D. Stanescu, S. Tewari, Robust low-energy Andreev bound states in semiconductor-superconductor structures: importance of partial separation of component Majorana bound states. Phys. Rev. B **100**, 155429 (2019). https://doi.org/10.1103/PhysRevB.100.155429
21. C.-X. Liu, J.D. Sau, S. Das Sarma, Distinguishing topological Majorana bound states from trivial Andreev bound states: proposed tests through differential tunneling conductance spectroscopy. Phys. Rev. B **97**, 214502 (2018). https://doi.org/10.1103/PhysRevB.97.214502
22. E. Prada, P. San-Jose, M.W.A. de Moor, A. Geresdi, E.J.H. Lee, J. Klinovaja, D. Loss, J. Nygård, R. Aguado, L.P. Kouwenhoven, From Andreev to Majorana bound states in hybrid superconductor–semiconductor nanowires. Nat. Rev. Phys. **2**, 575 (2020). https://doi.org/10.1038/s42254-020-0228-y
23. M. Hell, K. Flensberg, M. Leijnse, Distinguishing Majorana bound states from localized Andreev bound states by interferometry. Phys. Rev. B **97**, 161401 (2018). https://doi.org/10.1103/PhysRevB.97.161401
24. P. Yu, J. Chen, M. Gomanko, G. Badawy, E.P.A.M. Bakkers, K. Zuo, V. Mourik, S.M. Frolov, Non-Majorana states yield nearly quantized conductance in proximatized nanowires. Nat. Phys. **17**, 482 (2021). https://doi.org/10.1038/s41567-020-01107-w
25. M. Aghaee et al., InAs-Al hybrid devices passing the topological gap protocol. Phys. Rev. B **107**, 245423 (2023). https://doi.org/10.1103/PhysRevB.107.245423
26. T. Oka, S. Kitamura, Floquet engineering of quantum materials. Annu. Rev. Condens. Matter Phys. **10**, 387 (2019). https://doi.org/10.1146/annurev-conmatphys-031218-013423
27. C. Weitenberg, J. Simonet, Tailoring quantum gases by floquet engineering. Nat. Phys. **17**, 1342 (2021). https://doi.org/10.1038/s41567-021-01316-x
28. J. Smits, L. Liao, H.T.C. Stoof, P. van der Straten, Observation of a space-time crystal in a superfluid quantum gas. Phys. Rev. Lett. **121**, 185301 (2018). https://doi.org/10.1103/PhysRevLett.121.185301
29. K. Sacha, J. Zakrzewski, Time crystals: a review. Rep. Prog. Phys. **81**, 016401 (2017). https://doi.org/10.1088/1361-6633/aa8b38

30. M.S. Rudner, N.H. Lindner, Band structure engineering and non-equilibrium dynamics in floquet topological insulators. Nat. Rev. Phys. **2**, 229 (2020). https://doi.org/10.1038/s42254-020-0170-z

31. S. Kitamura, H. Aoki, Floquet topological superconductivity induced by chiral many-body interaction. Commun. Phys. **5**, 174 (2022). https://doi.org/10.1038/s42005-022-00936-w

32. R.-X. Zhang, S. Das Sarma, Anomalous floquet chiral topological superconductivity in a topological insulator sandwich structure. Phys. Rev. Lett. **127**, 067001 (2021). https://doi.org/10.1103/PhysRevLett.127.067001

33. A.C. Potter, T. Morimoto, A. Vishwanath, Classification of interacting topological floquet phases in one dimension. Phys. Rev. X **6**, 041001 (2016). https://doi.org/10.1103/PhysRevX.6.041001

34. T. Kitagawa, E. Berg, M. Rudner, E. Demler, Topological characterization of periodically driven quantum systems. Phys. Rev. B **82**, 235114 (2010). https://doi.org/10.1103/PhysRevB.82.235114

35. F. Harper, R. Roy, M.S. Rudner, S. Sondhi, Topology and broken symmetry in floquet systems. Annu. Rev. Condens. Matter Phys. **11**, 345 (2020). https://doi.org/10.1146/annurev-conmatphys-031218-013721

36. G. Engelhardt, J. Cao, Dynamical symmetries and symmetry-protected selection rules in periodically driven quantum systems. Phys. Rev. Lett. **126**, 090601 (2021). https://doi.org/10.1103/PhysRevLett.126.090601

37. G. Wang, C. Li, P. Cappellaro, Observation of symmetry-protected selection rules in periodically driven quantum systems. Phys. Rev. Lett. **127**, 140604 (2021). https://doi.org/10.1103/PhysRevLett.127.140604

38. B. Min, B. Fajardo, T. Pereg-Barnea, K. Agarwal, Dynamical approach to improving Majorana qubits and distinguishing them from trivial bound states. Phys. Rev. B **105**, 155412 (2022). https://doi.org/10.1103/PhysRevB.105.155412

39. E. Prada, R. Aguado, P. San-Jose, Measuring Majorana nonlocality and spin structure with a quantum dot. Phys. Rev. B **96**, 085418 (2017). https://doi.org/10.1103/PhysRevB.96.085418

40. D.J. Clarke, Experimentally accessible topological quality factor for wires with zero energy modes. Phys. Rev. B **96**, 201109 (2017). https://doi.org/10.1103/PhysRevB.96.201109

41. B. Baran, T. Domański, Quasiparticles of a periodically driven quantum dot coupled between superconducting and normal leads. Phys. Rev. B **100**, 085414 (2019). https://doi.org/10.1103/PhysRevB.100.085414

42. B. Baran, R. Taranko, T. Domański, Subgap dynamics of double quantum dot coupled between superconducting and normal leads. Sci. Rep. **11**, 11138 (2021). https://doi.org/10.1038/s41598-021-90080-2

43. C. Ortega-Taberner, A.-P. Jauho, J. Paaske, Anomalous Josephson current through a driven double quantum dot. Phys. Rev. B **107**, 115165 (2023). https://doi.org/10.1103/PhysRevB.107.115165

44. A. Keliri, B. Douçot, Driven Andreev molecule. Phys. Rev. B **107**, 094505 (2023). https://doi.org/10.1103/PhysRevB.107.094505

45. F.M.C. Damanet, E. Mascarenhas, D. Pekker, A.J. Daley, Controlling quantum transport via dissipation engineering. Phys. Rev. Lett. **123**, 180402 (2019). https://doi.org/10.1103/PhysRevLett.123.180402

46. M. Cheng, M. Becker, B. Bauer, R.M. Lutchyn, Interplay between Kondo and Majorana interactions in quantum dots. Phys. Rev. X **4**, 031051 (2014). https://doi.org/10.1103/PhysRevX.4.031051

47. G. Górski, J. Barański, I. Weymann, T. Domański, Interplay between correlations and Majorana mode in proximitized quantum dot. Sci. Rep. **8**, 15717 (2018). https://doi.org/10.1038/s41598-018-33529-1

48. A.Y. Kitaev, Unpaired Majorana fermions in quantum wires. PHYS-USP+ **44**, 131 (2001). https://doi.org/10.1070/1063-7869/44/10S/S29

49. J. Danon, E.B. Hansen, K. Flensberg, Conductance spectroscopy on Majorana wires and the inverse proximity effect. Phys. Rev. B **96**, 125420 (2017). https://doi.org/10.1103/PhysRevB.96.125420

50. L.S. Ricco, V.L. Campo, I.A. Shelykh, A.C. Seridonio, Majorana oscillations modulated by Fano interference and degree of nonlocality in a topological superconducting-nanowire-quantum-dot system. Phys. Rev. B **98**, 075142 (2018). https://doi.org/10.1103/PhysRevB.98.075142

51. M.-T. Deng, S. Vaitiekėnas, E. Prada, P. San-Jose, J. Nygård, P. Krogstrup, R. Aguado, C.M. Marcus, Nonlocality of Majorana modes in hybrid nanowires. Phys. Rev. B **98**, 085125 (2018). https://doi.org/10.1103/PhysRevB.98.085125

52. L.S. Ricco, Y. Marques, J.E. Sanches, I.A. Shelykh, A.C. Seridonio, Interaction induced hybridization of Majorana zero modes in a coupled quantum-dot-superconducting-nanowire hybrid system. Phys. Rev. B **102**, 165104 (2020). https://doi.org/10.1103/PhysRevB.102.165104

53. F. Medina, J.P. Ramos-Andrade, L. Rosales, P. Orellana, Influence of Majorana bound states in quantum rings. Ann. Phys. **532**, 2000199 (2020). https://doi.org/10.1002/andp.202000199

54. B.H. Wu, J.C. Cao, C. Timm, Polaron effects on the dc- and ac-tunneling characteristics of molecular Josephson junctions. Phys. Rev. B **86**, 035406 (2012). https://doi.org/10.1103/PhysRevB.86.035406

55. N. Tsuji, T. Oka, H. Aoki, Correlated electron systems periodically driven out of equilibrium: Floquet + DMFT formalism. Phys. Rev. B **78**, 235124 (2008). https://doi.org/10.1103/PhysRevB.78.235124

56. Q.-F. Sun, J. Wang, T.-H. Lin, Resonant Andreev reflection in a normal-metal-quantum-dot-superconductor system. Phys. Rev. B **59**, 3831 (1999). https://doi.org/10.1103/PhysRevB.59.3831

57. Q.-B. Zeng, S. Chen, L. You, R. Lü, Transport through a quantum dot coupled to two Majorana bound states. Front. Phys. **12**, 127302 (2016). https://doi.org/10.1007/s11467-016-0620-3

58. A. Schuray, L. Weithofer, P. Recher, Fano resonances in Majorana bound states-quantum dot hybrid systems. Phys. Rev. B **96**, 085417 (2017). https://doi.org/10.1103/PhysRevB.96.085417

59. T. Zhou, M.C. Dartiailh, K. Sardashti, J.E. Han, A. Matos-Abiague, J. Shabani, I. Žutić, Fusion of Majorana bound states with mini-gate control in two-dimensional systems. Nat. Commun. **13**, 1738 (2022). https://doi.org/10.1038/s41467-022-29463-6

60. Z. Wang, W.-C. Huang, Q.-F. Liang, X. Hu, Landau–Zener–Stückelberg interferometry for majorana qubit. Sci. Rep. **8**, 7920 (2018). https://doi.org/10.1038/s41598-018-26324-5

61. W.-C. Huang, Q.-F. Liang, D.-X. Yao, Z. Wang, Manipulating the Majorana qubit with Landau–Zener–Stückelberg interference. Phys. Rev. A **92**, 012308 (2015). https://doi.org/10.1103/PhysRevA.92.012308

62. R. Taranko, T. Kwapiński, T. Domański, Transient dynamics of a quantum dot embedded between two superconducting leads and a metallic reservoir. Phys. Rev. B **99**, 165419 (2019). https://doi.org/10.1103/PhysRevB.99.165419

63. J. Avila, F. Peñaranda, E. Prada, P. San-Jose, R. Aguado, Non-equilibrium topology as a unifying framework for the Andreev versus Majorana states controversy. Commun. Phys. **2**, 133 (2019). https://doi.org/10.1038/s42005-019-0231-8

64. L. Zhou, Non-hermitian floquet topological superconductors with multiple Majorana edge modes. Phys. Rev. B **101**, 014306 (2020). https://doi.org/10.1103/PhysRevB.101.014306